POLITECNICO DI TORINO
Repository ISTITUZIONALE

Integrated PCB-to-Waveguide Feed Element for Ka-Band Active Antennas in Dual-Circular Polarization

Original
Integrated PCB-to-Waveguide Feed Element for Ka-Band Active Antennas in Dual-Circular Polarization / Montoya-Roca, R., Vazquez-Sogorb, C., Paonessa, F., Lumia, M., Addamo, G., Peverini, O., Maiarelli, D., Virone, G.. - In: IEEE JOURNAL OF MICROWAVES. - ISSN 2692-8388. - ELETTRONICO. - (2026). [10.1109/JMW.2026.3745730]

Availability:
This version is available at: 11583/3018092 since: 2026-11-17T23:43:05Z

Publisher:
IEEE

Published
DOI:10.1109/JMW.2026.3745730

Terms of use:

This article is made available under terms and conditions as specified in the corresponding bibliographic description in the repository

Publisher copyright

(Article begins on next page)

29 November 2026

This article has been accepted for inclusion in a future issue of this journal. Content is final as presented, with the exception of pagination.

IEEE Journal of Microwaves

Received 7 May 2026; revised 5 September 2026; accepted 12 October 2026.

Digital Object Identifier 10.1109/JMW.2026.3745730

Integrated PCB-to-Waveguide Feed Element for Ka-Band Active Antennas in Dual-Circular Polarization

ROGER MONTOYA-ROCA [1,2] (Member, IEEE), CARLOS VAZQUEZ-SOGORB [1,2] (Graduate Student Member, IEEE), FABIO PAONESSA [1] (Member, IEEE), MAURO LUMIA [1] (Member, IEEE), GIUSEPPE ADDAMO [1] (Member, IEEE), OSCAR A. PEVERINI [1] (Member, IEEE), DAVIDE MAIARELLI [3] (Member, IEEE), AND GIUSEPPE VIRONE [1] (Senior Member, IEEE)

(Regular Paper)

[1]Istituto di Elettronica e di Ingegneria dell'Informazione e delle Telecomunicazioni (IEIIT), Consiglio Nazionale delle Ricerche (CNR), 10129 Turin, Italy
[2]Department of Electronics and Telecommunications, Politecnico di Torino, 10129 Turin, Italy
[3]Thales Alenia Space, 00131 Rome, Italy

CORRESPONDING AUTHOR: Roger Montoya-Roca (e-mail: rogermontoyaroca@cnr.it).

This work was supported by European Union, through ANTERRA 101072363 HORIZON-MSCA-2021-DN-01.

ABSTRACT This paper presents a novel compact PCB-to-waveguide feed element enabling dual-circular polarization for full-metal direct radiating arrays operating in the Ka-band downlink (17.7 − 20.7 GHz). The proposed solution is based on an end-launcher that allows the direct and simultaneous excitation of the two orthogonal linearly-polarized modes in a three-ridge hexagonal waveguide from PCB. A three-ridge hexagonal waveguide polarizer then introduces the 90° phase shift to generate the circular polarization. The proposed design effectively addresses the limitations of conventional in-line waveguide end-launchers reported in the literature, which are typically confined to single-mode or single-polarization excitation. Another significant advantage for large-scale integration is the absence of ohmic contact between the PCB excitation pin and the metal waveguide. The developed feed element provides a compact alternative to septum polarizers and waveguide orthomode transducers. The overall length is less than 26 mm. A seven-element array prototype was fabricated and experimentally characterized to validate the design. The measured results are in good agreement with full-wave simulations, showing reflection and isolation levels of −15 dB and −18 dB, respectively, XPD above 30 dB and insertion loss less than 0.6 dB.

INDEX TERMS Antenna feeds, direct radiating arrays, dual-circular polarization, horn antennas, Ka-band, low Earth orbit satellites, microstrip-to-waveguide transition, PCB-to-waveguide transition, phased array antenna, ridged waveguide apertures, satellite antennas, satellite communications, septum polarizer, waveguide components, waveguide end-launcher, waveguide feed element, waveguide polarizer.

I. INTRODUCTION

Direct radiating arrays (DRAs) have emerged as an excellent antenna candidate for low Earth orbit (LEO) satellite communication in the Ku- and Ka-bands. These antennas enable electronic steering of multiple beams without the need for mechanical movement, offering fast beam switching and adaptive beamforming capabilities that ensure flexible and high-reliable connectivity [1]. Furthermore, their compact and low-profile design makes them particularly well-suited for space applications.

Dual-polarized radiating elements capable of generating both left-hand circular polarization (LHCP) and right-hand circular polarization (RHCP) are essential to increase system capacity. Ridged waveguide apertures, offering an all-metal solution, are explored nowadays due to their low losses, excellent power handling capabilities, and inherent operability

© 2026 The Authors. This work is licensed under a Creative Commons Attribution 4.0 License. For more information, see https://creativecommons.org/licenses/by/4.0/

This article has been accepted for inclusion in a future issue of this journal. Content is final as presented, with the exception of pagination.

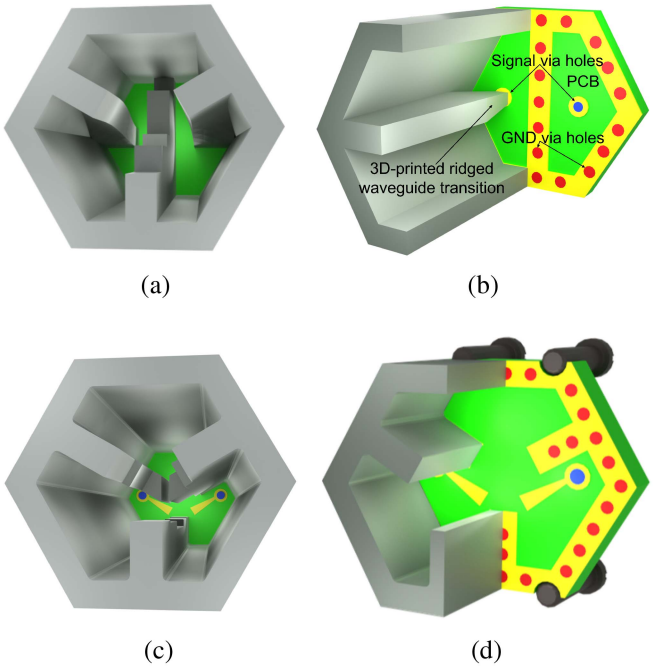

FIGURE 1. (a) Sketch of the feed element proposed in [8], (b) the corresponding longitudinal cut-view of the 3D-printed coaxial pin end-launcher (sketch from [8]), (c) the proposed PCB-to-waveguide feed element, and (d) the longitudinal cut-view of the proposed dual-pol end-launcher.

in harsh environments [2], [3]. Ridged hexagonal and circular waveguide apertures arranged in a triangular lattice configuration are currently under research as a promising solution [4], [5], [6]. Their advantage lies in a broader single-mode bandwidth and a larger effective aperture area compared to ridged square waveguide apertures.

The design of dual-mode feed elements that integrate such high-performance apertures with electronics is challenging due to the severe spacing constraints between elements [7]. In the literature, ridged waveguide radiating elements use a septum polarizer (see Fig. 1(a)) to convert the fundamental modes at the two single-mode ridged ports to circular polarizations at the common port [8]. As shown in Fig. 1(b), the excitation of the single-mode ridged ports feature a tapered 3D-printed transition from the corresponding signal via holes on the PCB (blue). Such via holes are connected to either coaxial connectors or printed transmission lines on the back of the PCB for direct integration of the front-end electronics. The other red vias (named as ground GND vias) and the corresponding yellow metallization extend the waveguide sections towards the ground plane on the back of the PCB. The 3D-printed transitions to signal vias in Fig. 1(b) require a good mechanical and electrical contact, which is difficult to achieve in large-scale production due to the overall manufacturing and assembly uncertainties.

In this work, we present an alternative solution that does not require such a contact between signal vias and the metallic waveguide parts. As shown in Fig. 1(c) and (d), printed monopoles are used to excite two orthogonal modes in the three-ridge common waveguide. This innovative solution, hereafter referred to as dual-pol end-launcher, can be considered as a compact PCB version of the asymmetric waveguide orthomode transducer (OMT) presented in [9]. It is worth to mention that the dual-pol end-launcher configuration in Fig. 1(d) does not make use of an evanescent-wave section [10] between PCB and waveguide. A good performance in terms of both reflection and isolation is achieved by both designing the monopole shape and selecting a suitable thickness and permittivity of the PCB only. In this way, additional matching sections are not required. Moreover, differently from [10], the crossing of monopoles (coupling pads) is avoided to allow a simple and compact double-layer PCB implementation.

We also introduce a three-ridge polarizer configuration to achieve the desired 90° phase shift. Differently from other ridge-based polarizers reported in [11], [12], the three-ridge configuration presented in this work achieves the required 90° phase shift by combining both positive and negative variations of the ridge height with respect to the input/output sections (see Fig. 1(c)). This configuration was conceived to minimize the overall length of the feed element.

The paper is organized as follows. Section II presents the design and performance of the PCB-to-three-ridge hexagonal waveguide dual-pol end-launcher. Section III describes the design methodology and the simulations of the waveguide polarizer. In addition, the performance of the complete feed element is presented. Section IV describes the seven-element array prototype and its experimental validation through back-to-back and extended through short-delay technique measurements in both dual-linear and circular polarization [13]. Finally, Section V summarizes the conclusions of this work.

II. PCB-TO-THREE-RIDGE HEXAGONAL WAVEGUIDE END-LAUNCHER: DESIGN AND ANALYSIS

A. DRA DESIGN FOR LEO SATCOM

The primary requirements for DRAs are good impedance matching and high polarization purity over a beam scanning range of $\pm 50^\circ - \pm 60^\circ$ [14]. To prevent the appearance of grating lobes within the desired field of view (FoV), the element spacing, or periodicity (P), is selected according to the grating lobe-free condition [15] for infinite arrays, expressed by (1).

$$\frac{P}{\lambda} \leq \frac{1}{\sin\theta_L} \frac{1}{1+\sin\theta_S} \tag{1}$$

where θ_L defines the lattice angle (60° for triangular lattice) and θ_S denotes the maximum scan angle.

According to (1), and considering the highest frequency of the band (20.7 GHz) with a maximum scan limit of 60°, the corresponding element period is calculated to be 8.96 mm ($P = 0.62\lambda$).

B. DUAL-POL END-LAUNCHER DESIGN

Fig. 2(a) illustrates the proposed PCB-to-three-ridge hexagonal waveguide end-launcher in an array configuration. To

This article has been accepted for inclusion in a future issue of this journal. Content is final as presented, with the exception of pagination.

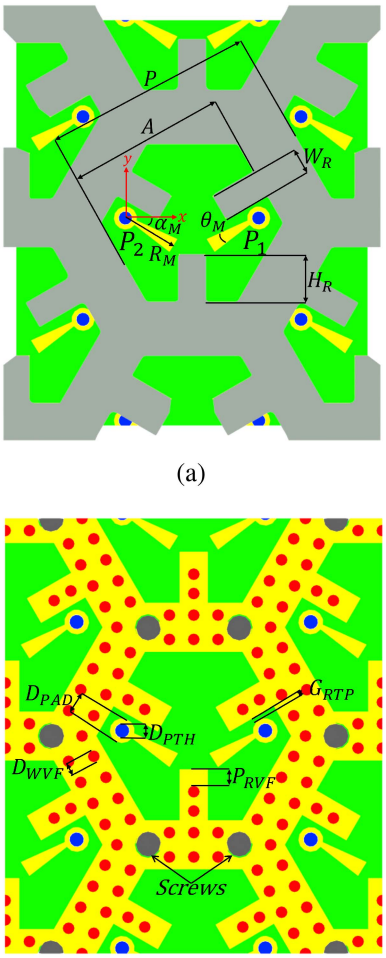

FIGURE 2. (a) Front view of the proposed PCB-to-three-ridge hexagonal waveguide end-launcher in an array configuration and (b) front view with the metallic waveguide section removed.

ensure proper mechanical manufacturing and assembly, the waveguide aperture (A) must be smaller than the array period ($A \leq P$). A minimum metal wall thickness of 2 mm ($P - A$) was chosen to accommodate mounting screw holes (dark gray circles in Fig. 2(b)). This solution ensures proper mechanical and electrical connection between PCB ground metallization (yellow region with red vias) and waveguide (gray region in Fig. 2(a)). The PCB substrate is depicted in green. Consequently, the maximum allowable waveguide aperture A is 6.96 mm.

The ridge height (H_R) and width (W_R) are carefully selected to ensure that the waveguide operates above cut-off, with sufficient margin to the lower end of the operative frequency band (17.7 GHz). The cut-off frequency of the fundamental modes is 16.5 GHz (see Fig. 5) whereas the first higher-order mode is 35.2 GHz.

Fig. 2(b) shows the PCB feeding structure, highlighting the main design dimensions. GND via holes with diameter (D_{WVF}) are implemented to extend the three-ridge hexagonal waveguide through the PCB towards its back metallization, thereby creating a back-short. These via holes are designed to minimize isolation between adjacent elements by maintaining an inter-via spacing of less than $\lambda/10$ at the highest operational frequency, ensuring effective isolation between the elements (residual coupling is negligible).

The overall structure, composed of dielectric substrate and via holes, is designed to operate as a quarter-wave waveguide section that transforms the short-circuit provided by the PCB back metallization to an open circuit at the monopole level. In this way, such coupling structures radiate only towards the metal waveguide. The Rogers RO4350B substrate ($\epsilon_r = 3.66$, $\tan\delta = 0.0037$) was selected since it is space qualified and presents low losses. After a few design iterations, a standard thickness of 1.52 mm [16] was selected as the optimum value among available options. The via holes that are placed at a distance of (P_{RVF}) from the ridge edge were also part of the optimization. This added more degrees of freedom to compensate for the limited availability of substrate thickness.

On the top layer of the PCB, the monopole in P1 (P2) with radial geometry [17] is properly placed and designed to excite the fundamental mode of the three-ridge hexagonal waveguide (common port) that is oriented along U (V) (see Fig. 3(a)). This modal configuration is necessary to properly feed the waveguide polarizer described in Section III [18]. In the framework of the design procedure presented in this section, the U and V modes are decomposed as the sum and difference of M_X and M_Y that are visible in Fig. 3(b) and (c), respectively (M_X and M_Y are also the principal polarizations of the polarizer, see Section III). In this way, the excitation of the fundamental mode polarized along U (V) is equivalent to the simultaneous excitation of M_X and M_Y with equal amplitude and same (opposite) phase. It should be noted that such 0° and 180° phase difference comes from the geometry itself. The corresponding ports definition for the dual-pol end-launcher is shown in Fig. 4(a).

With reference to Fig. 2(a), the design parameters of the monopoles are θ_M and α_M, i.e the angular width and rotation angle, and the radius R_M. The monopoles are fed through the signal via holes depicted with blue in Fig 2. Such via holes are implemented as plated through-holes (PTHs) with diameter D_{PTH}. Finally, D_{PAD} is the diameter of the surrounding pads. As it is shown in Section IV, the PTHs accommodate the inner pin of the Sub-Miniature Push-on Micro (SMPM) Bulkhead Plug Hermetic Sealed connectors that are soldered on the back of the PCB. In the simulations, such connectors are modeled up to the Corning 7070 glass section. The design parameters of the dual-pol end-launcher are listed in Table 1.

C. PARAMETRIC ANALYSES

The simulated results presented in this work were obtained using CST Microwave Studio. The most relevant parametric analyses are discussed hereafter to both justify the values reported in Table 1 and to further outline the design flow.

The reflection and isolation for different combinations of ridge parameters H_R and W_R are reported in Figs. 5 and 6, respectively.

This article has been accepted for inclusion in a future issue of this journal. Content is final as presented, with the exception of pagination.

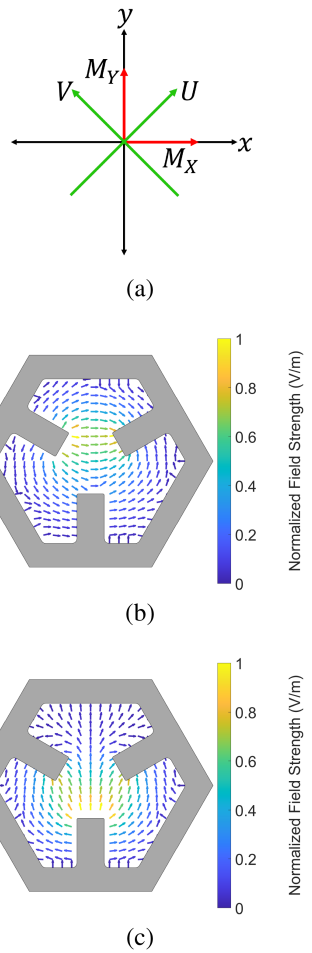

FIGURE 3. Electric field distribution of the fundamental modes in the three-ridge waveguide (common port): (a) reference system showing the E-field polarization of the U-V fundamental modes excited by the monopoles and their decomposition in M_X and M_Y, (b) E-field of mode M_X, polarized along the x-axis, and (c) E-field of mode M_Y, polarized along the y-axis.

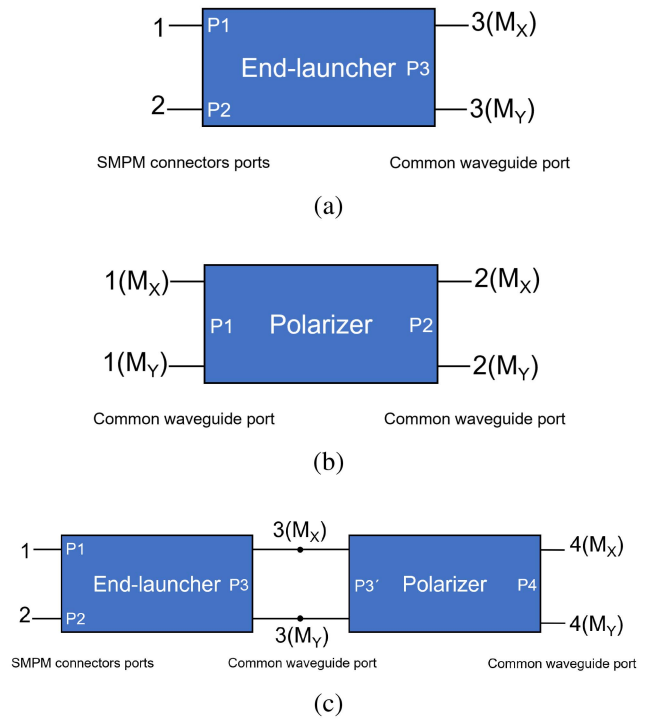

FIGURE 4. Port definition: (a) end-launcher, (b) polarizer, and (c) complete feed element.

TABLE 1. End-Launcher Geometrical Design Parameters

Parameter	Description	Value (mm)
P	Waveguide Period	8.96
A	Waveguide Aperture	6.96
H_R	Ridge height	2.1
W_R	Ridge width	1.15
T_S	Substrate thickness	1.52
D_{PTH}	PTH drill diameter	0.6
D_{PAD}	Pad diameter	1
D_{WVF}	GND via diameter	0.5
θ_M	Monopole angular width (°)	15
α_M	Monopole rotation angle (°)	24.4
R_M	Monopole radius	1.94
G_{RTP}	Gap ridge to pad	0.21
P_{RVF}	Position GND via to ridge edge	0.66

As shown in Fig. 5, the cut-off frequency is driven by the ridge height H_R. For example, H_R equal to 2 mm (blue curves) and 2.1 mm (red curves) provide a cut-off frequency around 17 GHz and 16.5 GHz, respectively. H_R values below 2 mm do not provide a sufficient margin from the lower end of the band (17.7 GHz). It should be also noted that higher values of H_R shift the first resonance of the reflection coefficient toward lower frequencies, improving the matching at the lower end of the band. On the contrary, with reference to Fig. 6, high values of H_R impair the isolation performance because the spacing between the monopoles and ridges is reduced.

As far as W_R is concerned, a minimum value of 1 mm is required due to manufacturing constraints. As presented in Fig. 6, the most significant effect of W_R is the degradation of the isolation for higher values (dotted curves). Starting from these considerations, the values of $H_R = 2.1$ mm and a $W_R = 1.15$ mm (black solid curve with dot markers) were selected as optimal trade-off values.

The impact of the monopole parameters on the scattering performances are reported in Figs. 7, 8, 9 and 10. The parameter R_M has a significant effect on the reflection coefficient because it controls the coupling to each fundamental mode. According to Fig. 7, $R_M = 1.9$ mm (green curve) and $R_M = 2$ mm (cyan curve) provide reflection coefficients lower than -17 dB. Smaller radii result in poorer impedance

This article has been accepted for inclusion in a future issue of this journal. Content is final as presented, with the exception of pagination.

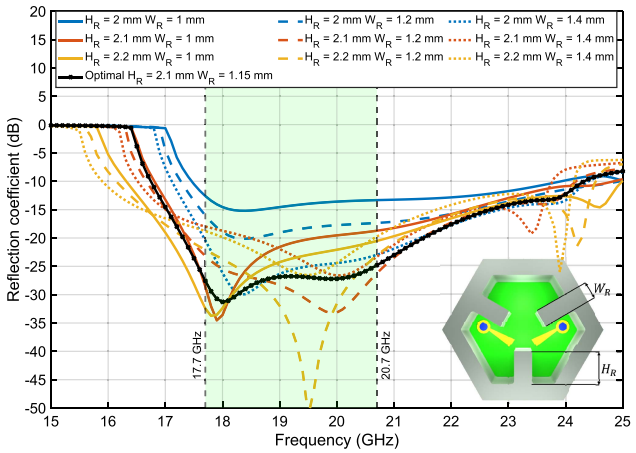

FIGURE 5. Impact of ridge parameters H_R and W_R on the reflection coefficient (S_{11}). The light green region between the dashed black lines indicates the operative band.

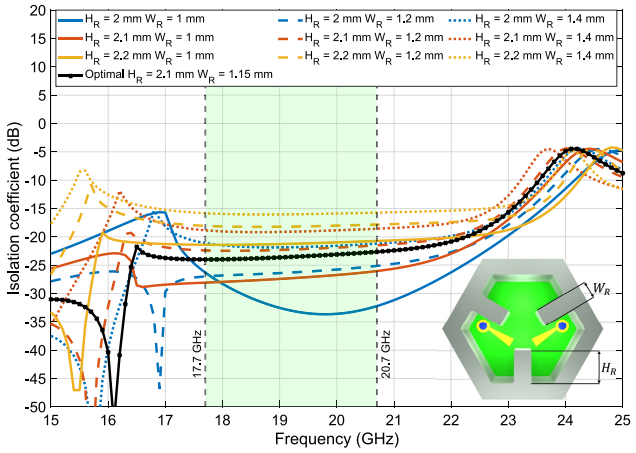

FIGURE 6. Impact of ridge parameters H_R and W_R on the isolation coefficient (S_{21}).

matching. Based on this analysis, a radius of $R_M = 1.94$ mm was achieved as the optimal value.

The monopole orientation angle α_M produces a more complex effect that impacts both reflection and transmission coefficients. In Fig. 8, values of α_M between 20° and 30° improve the impedance matching due to the appearance of two distinct resonances that broaden the bandwidth. Figs. 9 and 10 show that α_M directly controls the transmission ratio between modes M_X and M_Y in both magnitude and phase. Results from excitation on port 2 (not shown) provide similar behavior centered around 180°. The suitable range is identified as 20°−25° (purple and green curves). It has been found that a value of $\alpha_M = 24.4°$ provides the best compromise between reflection minimization and transmission equalization.

The other parameters such as via fences position and monopole angular width θ_M are not discussed because their effect is less significant in the overall performance.

As mentioned above, the design has been performed in the M_X and M_Y basis because these are the principal polarizations of the polarizer. Equation. (2) and (3) define the transmission ($S_{3(U)1}, S_{3(V)2}$) and cross-coupling ($S_{3(V)1}, S_{3(U)2}$) coefficients

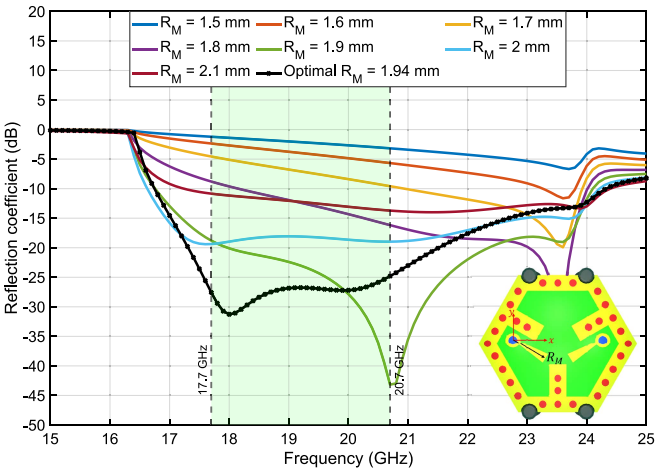

FIGURE 7. Impact of the monopole radius R_M on the reflection coefficient.

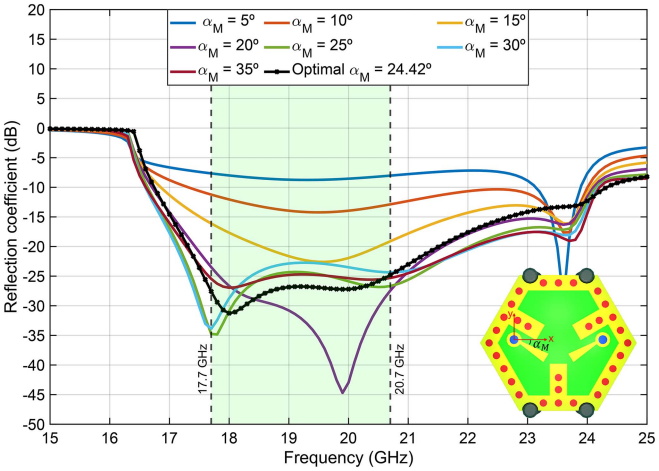

FIGURE 8. Impact of the rotation angle α_M on the reflection coefficient.

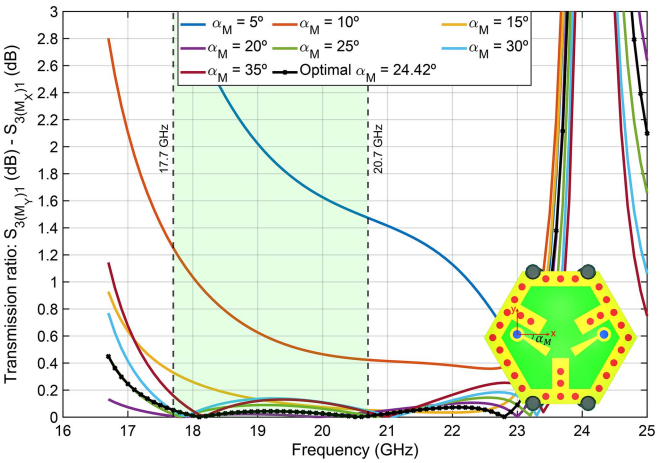

FIGURE 9. Impact of the rotation angle α_M on the magnitude of transmission ratio between fundamental modes M_X and M_Y at the common port with excitation on coaxial port 1. Results below 16.5 GHz (cut-off frequency) are not shown.

This article has been accepted for inclusion in a future issue of this journal. Content is final as presented, with the exception of pagination.

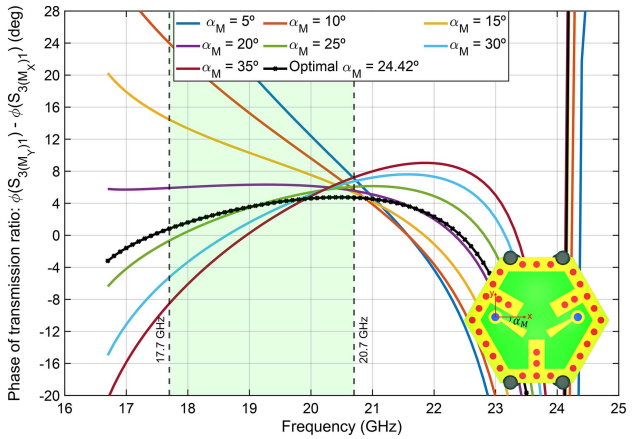

FIGURE 10. **Impact of the rotation angle α_M on the phase of transmission ratio between fundamental modes M_X and M_Y at the common port with excitation on coaxial port 1. Results below 16.5 GHz (cut-off frequency) are not shown.**

in the U/V basis that will be used to show the end-launcher performance in Section IV.

$$S_{3(U)1} = \frac{S_{3(M_X)1} + S_{3(M_Y)1}}{\sqrt{2}}$$
$$S_{3(V)2} = \frac{S_{3(M_X)2} + S_{3(M_Y)2}}{\sqrt{2}} \quad (2)$$
$$S_{3(V)1} = \frac{S_{3(M_X)1} - S_{3(M_Y)1}}{\sqrt{2}}$$
$$S_{3(U)2} = \frac{S_{3(M_X)2} - S_{3(M_Y)2}}{\sqrt{2}} \quad (3)$$

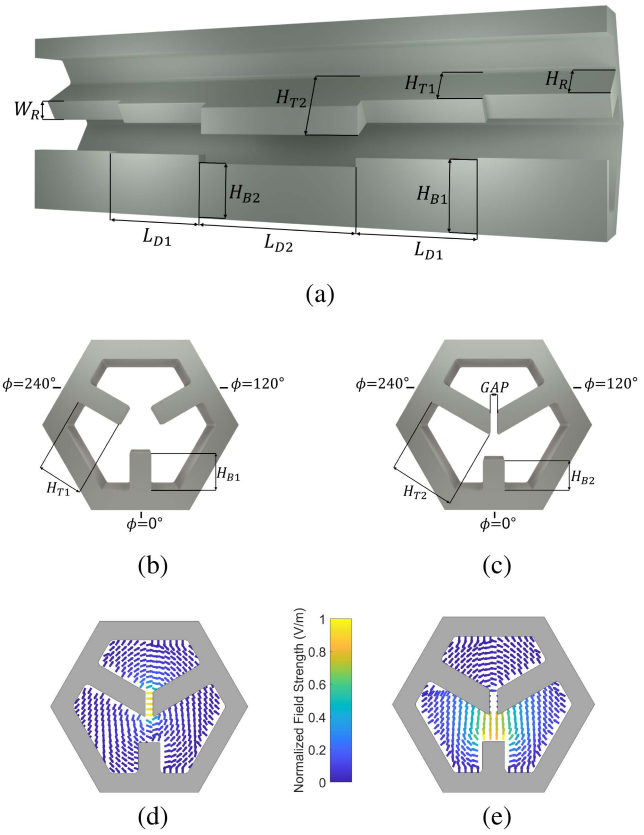

FIGURE 11. **(a) Longitudinal view of the three-ridge hexagonal waveguide polarizer, (b) front view of the first and third waveguide sections, (c) front view of the second waveguide section, (d) electric field distribution of M_X in the second waveguide section, and (e) electric field distribution of M_Y in the second waveguide section.**

III. THREE-RIDGE WAVEGUIDE POLARIZER

Coaxial port 1 (2) of the dual-mode end-launcher presented in Section II excites both fundamental modes M_X and M_Y (see Fig. 3) at the common port with equal magnitude and same (opposite) phase. The waveguide polarizer is hence required to introduce a 90° phase shift between such modes (also called principal polarizations) to provide dual circular polarization at the output port of the whole feed element [18].

A. THREE-RIDGE WAVEGUIDE POLARIZER DESIGN

A novel architecture of three-ridge hexagonal waveguide polarizer is shown in Fig. 11(a). It features input and output waveguide sections with the same dimensions (H_R, W_R and A) as the dual-mode end-launcher. This solution does not require additional transition sections, thereby preserving a compact and integrated architecture.

The whole polarizer consists of three one-fold symmetric waveguide sections (lengths L_{D1}, L_{D2} and $L_{D3} = L_{D1}$) whose transverse geometries are shown in Fig. 11(b) and (c). It can be appreciated that the heights of the ridges located at $\phi = 120°$ and $\phi = 240°$ (H_{T1} and H_{T2}, top ridges) are greater than the ones at $\phi = 0°$ (H_{B1} and H_{B2}, bottom ridges). As will be shown later, this configuration significantly decreases the cut-off frequency for M_X (because the field gets confined between ridges located at $\phi = 120°$ and $\phi = 240°$, see Fig. 11(d)). The variation of cut-off frequency is instead less significant for M_Y because the corresponding field (see Fig. 11(e)) is almost orthogonal to the top ridges. Therefore, this solution maximizes the difference between the propagation constants of M_X and M_Y, enabling a large differential phase shift per unit length. The latter leads to the achievement of the required 90° phase shift between M_X and M_Y with a compact structure.

With reference to Fig. 11, it can also be observed that the conceived structure combines both positive and negative stepped variations of the ridge height with respect to the input/output sections ($H_{T2} > H_{T1} > H_R$, whereas $H_{B2} < H_{B1} < H_R$).

In each waveguide section, the ridge dimensions must ensure operation above cut-off to allow proper mode propagation. The contour plots of the cut-off frequencies for the M_X and M_Y principal polarization modes are presented in Figs. 12 and 13, respectively, as a function of the top and bottom ridge heights (H_T and H_B). The light red regions in the bottom left corners correspond to below-cutoff condition. The orange regions visible in the top right corners instead enforce a minimum gap of 0.4 mm between the ridges, which is required to satisfy manufacturing constraints. As visible in Fig. 11(c),

This article has been accepted for inclusion in a future issue of this journal. Content is final as presented, with the exception of pagination.

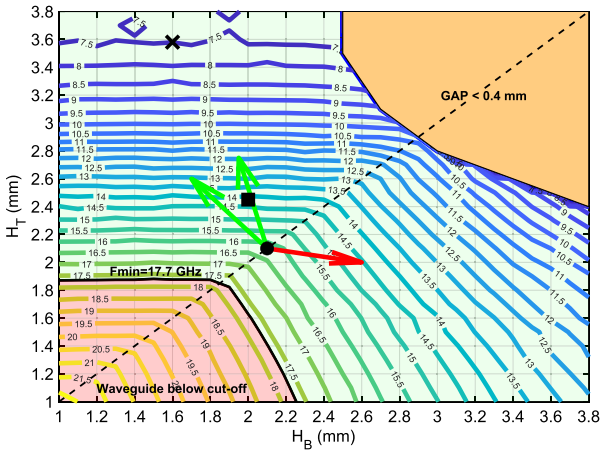

FIGURE 12. Cut-off frequency map for mode M_X with parameter combination of H_B and H_T.The dot is the ridge height of the input section (H_R), the square is the first and third waveguide sections (H_{B1}, H_{T1}) and the cross is the second (central) section (H_{B2}, H_{T2}).

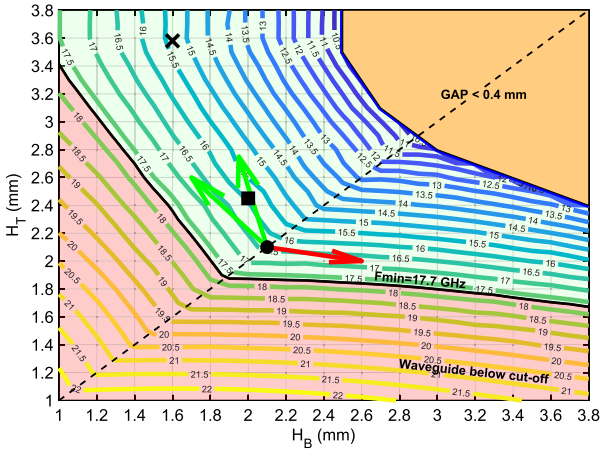

FIGURE 13. Cut-off frequency map for mode M_Y with parameter combination of H_B and H_T.

the geometry of the top ridges is modified (they present a trapezoidal shape) to accommodate such a gap. This modification allows greater values of H_T up to 3.8 mm avoiding the intersection of the ridges. The resulting light green regions identify the parameter space for which the waveguide operates above cut-off and manufacturing constraint is satisfied.

The parameter combination of the input/output section ($H_R = 2.1$ mm) is shown with the black dot that is placed on the diagonal dashed black line ($H_T = H_B$). As expected, the increase of either H_T or H_B (with respect to H_R) always reduces the cut-off frequency of both principal polarization modes (M_X and M_Y) reported in Figs. 12 and 13, respectively. However, as mentioned above, a differential phase shift per unit length $\varphi = k_z^Y - k_z^X$ is achieved when the two longitudinal propagation constants k_z^X and k_z^Y are different from each other. This aspect is clearly visible in Fig. 14 where the quantity φ is shown as a function of H_T and H_B. The differential phase shift φ is zero along the dashed black diagonal line ($H_T = H_B$). On the contrary, it is apparent that there are

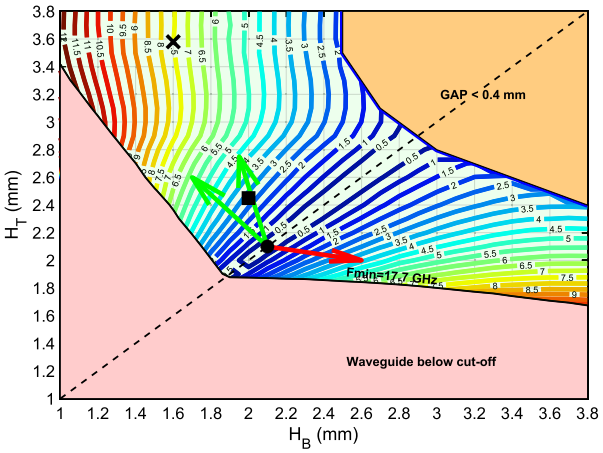

FIGURE 14. Differential phase shift per unit length φ (degrees/mm) at the central frequency (19 GHz) with parameter combination of H_B and H_T.

essentially two possible paths in the parameter space. Starting from the input ridge dimensions identified by the black dot, the first option (green arrows) consists of decreasing H_B while simultaneously increasing H_T. The second option (red arrow) instead involves increasing H_B while decreasing H_T.

As mentioned above, the cut-off and gap conditions impose significant constraints on the parameter space, considerably limiting the range of available parameter combinations. It can be noted that the parameter space is quite limited for the second option (red arrow). By comparing Figs. 13 and 14, it can also be noted that the first option (green arrows) enables high phase differences per unit length (e.g. 7.5°/mm, yellow curve) with a good margin with respect to the cut-off, see for example the parameter combination identified with the black cross (cut-off frequency at 15.5 GHz). This avoids significant degradation in both the matching performance and losses at the lower end of the band (17.7 GHz). In contrast, for the second option (red arrow), high phase differences per unit length (7.5°/mm, yellow curve) values are only obtained in proximity to the cut-off condition (cut-off frequency higher than 16.5 GHz).

All the considerations reported above led us to the selection of the green path as the optimal one for the design of the polarizer presented in this work. The first and second waveguide sections (L_{D1} and L_{D2}) are shown with black square and cross markers, respectively. Multi-objective optimization of the whole polarizer, considering both the reflection coefficient and the differential phase shift, yielded the final parameters reported in Table 2. The overall length of the polarizer ($2 \times L_{D1} + L_{D2}$) is 18.75 mm ($1.3\lambda_0$), offering a highly compact solution.

B. PERFORMANCE EVALUATION OF THE POLARIZER AND THE COMPLETE FEED ELEMENT

With reference to the black curve in Fig. 15, the designed polarizer introduces a differential phase shift of approximately 86.5° between the two principal polarizations (modes M_X and M_Y) at 19 GHz. This value is intentionally chosen to

This article has been accepted for inclusion in a future issue of this journal. Content is final as presented, with the exception of pagination.

TABLE 2. Waveguide Polarizer Geometrical Design Parameters

Parameter	Description	Value (mm)
H_R	Dual-pol end-launcher ridge height	2.1
W_R	Dual-pol end-launcher ridge width	1.15
H_{B1}	1 WG section: Bottom ridge height	2
H_{T1}	1 WG section: Top ridge height	2.45
H_{B2}	2 WG section: Bottom ridge height	1.6
H_{T2}	2 WG section: Top ridge height	3.58
L_{D1}	1 WG section length	5.3
L_{D2}	2 WG section length	8.15
GAP	Gap between ridges	0.4

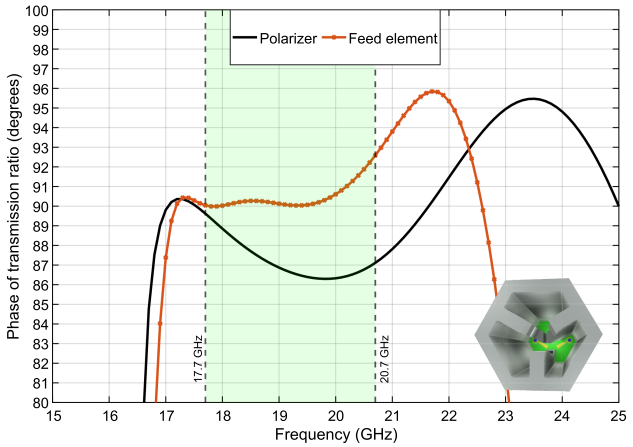

FIGURE 15. Differential phase shift between principal polarizations of the standalone polarizer and the feed element (with excitation on coaxial port 1).

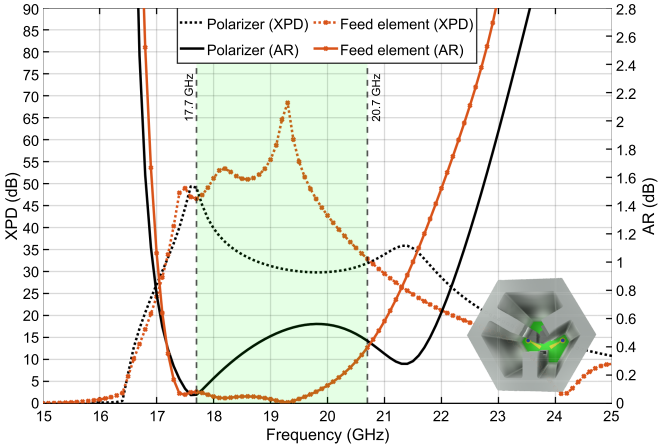

FIGURE 16. XPD and AR of the standalone polarizer and the feed element (with excitation on coaxial port 1).

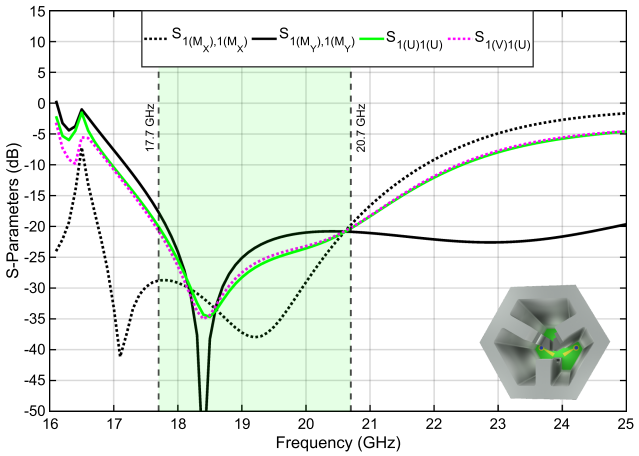

FIGURE 17. Reflection coefficients of the standalone polarizer in both the principal polarization (M_X and M_Y) and the U/V basis.

complement the additional 3.5° phase difference provided by the dual-pol end-launcher (see black curve with dot markers in Fig 10). As a consequence, the complete feed element in Fig. 15 provides a differential phase shift of 90° (red curve with dot markers). It can be appreciated that the differential phase shift of the whole feed element is very flat from 17.7 to 20.2 GHz (commercial Ka-band). This interesting performance is achieved because the positive slope of the dual-pol end-launcher (see Fig. 10) is compensating the negative slope of the polarizer. The residual ripple is due to multiple reflections inside the device. Eqs. (4) and (5) define the differential phase shift between the principal polarizations of the standalone polarizer and of the feed element when exciting port 1, respectively.

$$\phi_{(Polarizer)} = \phi(S_{2(M_Y)1(M_Y)}) - \phi(S_{2(M_X)1(M_X)}) \quad (4)$$

$$\phi_{(Feed\ element)} = \phi(S_{4(M_Y)1}) - \phi(S_{4(M_X)1}) \quad (5)$$

The corresponding cross-polarization discrimination (XPD) and axial ratio (AR) for the standalone polarizer and the feed element are shown in Fig. 16 with dotted and solid black and red curves, respectively. The standalone polarizer exhibits excellent polarization purity, with XPD values exceeding 30 dB and an AR consistently below 0.55 dB across the entire operating band. The feed element further improves performance, achieving XPD greater than 40 dB over most of the band and slightly decreasing to 33 dB near the upper edge, while maintaining an AR below 0.4 dB, thereby confirming the high polarization purity of the integrated design. Eqs. (6) and (7) define the XPD for standalone polarizer and feed element when exciting port 1, respectively.

$$XPD_{Polarizer} = \frac{S_{2(M_X)1(M_X)} + j \cdot S_{2(M_Y)1(M_Y)}}{S_{2(M_X)1(M_X)} - j \cdot S_{2(M_Y)1(M_Y)}} \quad (6)$$

$$XPD_{Feed\ element} = \frac{S_{4(M_X)1} + j \cdot S_{4(M_Y)1}}{S_{4(M_X)1} - j \cdot S_{4(M_Y)1}} \quad (7)$$

The simulated reflection coefficients for both principal polarizations of the polarizer defined in Fig. 4(b) are shown in Fig. 17 (black curves). The results demonstrate good reflection levels consistently below −17 dB across the operational

This article has been accepted for inclusion in a future issue of this journal. Content is final as presented, with the exception of pagination.

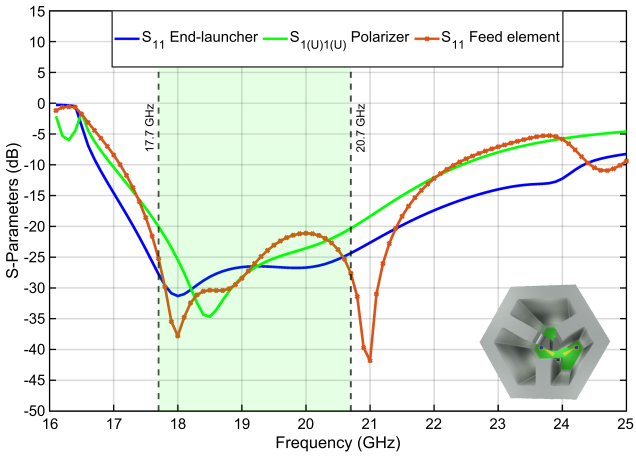

FIGURE 18. Reflection coefficient of the end-launcher, sum of the reflection coefficient of the polarizer in the U/V basis and reflection coefficient of the feed element (with excitation on coaxial port 1).

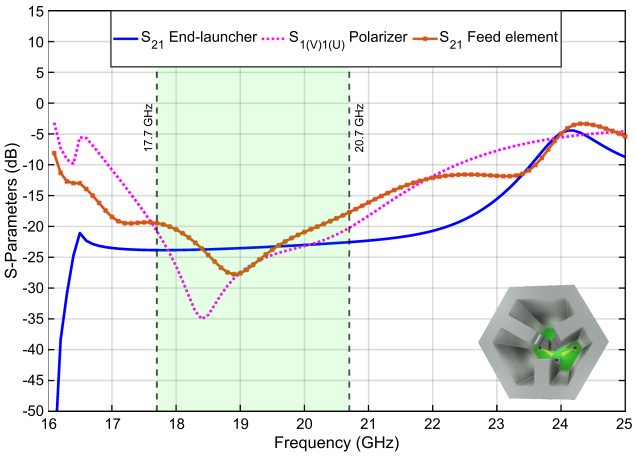

FIGURE 19. Isolation coefficient of the end-launcher, difference of the reflection coefficient of the polarizer in the U/V basis and isolation coefficient of the feed element (with excitation on coaxial port 1).

bandwidth. The performance in the U/V basis computed as

$$S_{1(U)1(U)} = S_{1(V)1(V)} = \frac{S_{1(M_X)1(M_X)} + S_{1(M_Y)1(M_Y)}}{\sqrt{2}}$$
$$S_{1(V)1(U)} = S_{1(U)1(V)} = \frac{S_{1(M_X)1(M_X)} - S_{1(M_Y)1(M_Y)}}{\sqrt{2}} \quad (8)$$

is instead shown with green and purple curves. Such curves are equal because a 90° phase shift (not shown for brevity) is present between $S_{1(M_X)1(M_X)}$ and $S_{1(M_Y)1(M_Y)}$. For the same reason, it can be also shown that

$$|S_{1(U)1(U)}| \approx |S_{1(V)1(U)}|$$
$$\approx \frac{\sqrt{|(S_{1(M_X)1(M_X)})|^2 + |S_{1(M_Y)1(M_Y)}|^2}}{\sqrt{2}} \quad (9)$$

This explains the lower value of $S_{1(U)1(U)}$ at 17.7 GHz (−20 dB, green curve), resulting from an $S_{1(Y)1(Y)}$ of −17 dB and $S_{1(M_X)1(M_X)}$ of −28 dB. The same reduction of about 3 dB occurs around 19.5 GHz where $S_{1(M_X)1(M_X)}$ is again negligible with respect to $S_{1(M_Y)1(M_Y)}$. The quantities $S_{1(U)1(U)}$ and $S_{1(V)1(U)}$ are also shown in Figs. 18 and 19, respectively, to justify the frequency response of the feed element, composed of both end-launcher and polarizer (see Fig. 4(c)).

The reflection and isolation coefficients of the complete feed element are presented in Figs. 18 and 19, respectively. The reflection coefficient (red solid curve with dot markers in Fig. 18) remains below −21 dB across the entire operating band. Such performance arises from the complex combination of the reflection of end-launcher (blue solid curve) and polarizer (green solid curve). A part from 20 GHz, where the two contributions add up providing a slightly higher mismatch, the combined performance is generally improved also showing a third resonance at 21 GHz. As far as the isolation coefficient is concerned (red solid curve with dot markers in Fig. 19), the combination of end-launcher and polarizer instead provides an overall performance that is slightly worse than the polarizer alone (purple dashed curve). Nevertheless, the feed element

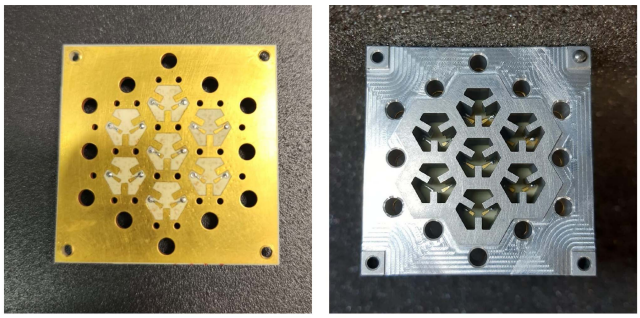

(a) (b)

FIGURE 20. (a) Front view of the PCB of the dual-pol end-launcher and (b) front view of the dual-pol end-launcher waveguide section.

isolation is below −20 dB up to 20.2 GHz, increasing to −18 dB towards 20.7 GHz.

The dual-pol end-launcher and polarizer are already co-designed to achieve a flat 90° differential phase shit with minimum overall length. Higher XPD, matching and isolation performance could be achieved by performing a joint optimization between them. The number of polarizer sections could also be increased at the expense of the overall length.

IV. SEVEN FEED ELEMENTS IN ARRAY CONFIGURATION

A. DESCRIPTION AND MANUFACTURING

A prototype with seven-feed elements in array configuration was manufactured to validate the design. The top layer of the PCB and the waveguide section of the dual-pol end-launcher are shown in Fig. 20(a) and (b), respectively. The overall dimensions is 4 cm × 4 cm. The complete array prototype including both dual-pol end-launcher and polarizer is presented in Fig. 21. The spacing between the elements is 8.96 mm, in agreement with the requirements reported in Section II(a).

The waveguide parts, which integrate the polarizer and the waveguide section of the dual-pol end-launcher, were fabricated using Electrical Discharge Machining (EDM) to achieve

This article has been accepted for inclusion in a future issue of this journal. Content is final as presented, with the exception of pagination.

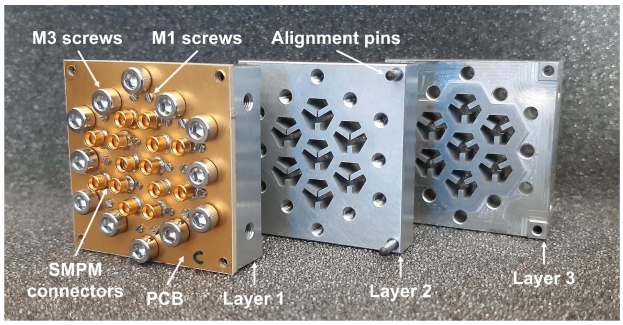

FIGURE 21. Profile view of the array prototype with seven dual-pol feed elements.

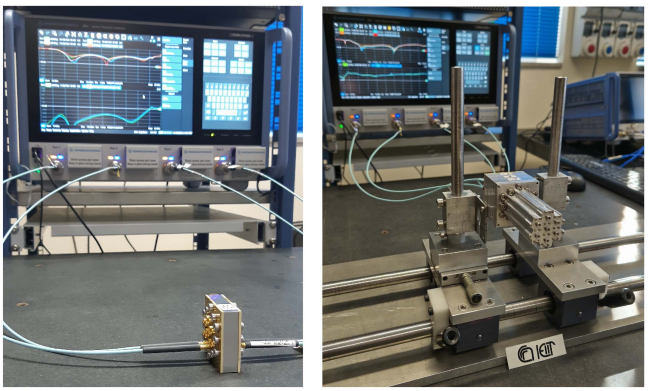

(a) (b)

FIGURE 22. (a) Back-to-back measurement setup and (b) measurement setup based on the method proposed in [13].

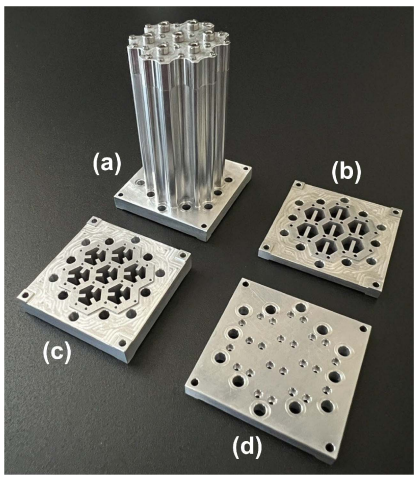

FIGURE 23. Waveguide calibration kit: (a) matched load, (b) reactive load, (c) $\lambda_{WG}/4$ waveguide section, and (d) short circuit.

low fabrication tolerances of the order of 10 μm. The device was manufactured in three separate layers to simplify the fabrication process [19]. Such a multilayer strategy has been already successfully verified up to W-band [20]. M1 screws were used to ensure reliable electrical contact between the top layer of the PCB (ground metallizations) and the first waveguide layer, which incorporates the end-launcher waveguide section and the first section of the polarizer. Central section of the polarizer is implemented in the second metal layer. The third layer, which is equal to the first one, includes the third polarizer section and the three-ridge common port. M3 screws, distributed around the seven feed elements, were used to provide mechanical fastening between the layers. Additionally, four alignment pins are located at the corners of the prototype to guarantee precise mechanical positioning and repeatable assembly.

A key advantage of the proposed architecture lies in the integration of the two SMPM connectors for each feed element within the available array inter-element spacing. In contrast to alternative approaches based on waveguide expander fanouts [21], [22], where the inter-element spacing is increased to accommodate the input coaxial ports, the proposed solution maintains the original inter-element spacing of the array without introducing additional transition stages, resulting in a more compact and scalable solution. Eliminating these intermediate structures significantly reduces mechanical complexity, minimizes insertion losses, and lowers both the overall weight and manufacturing cost. The presence of the SMPM connector for both polarizations facilitate the integration with other PCBs boards containing beamforming and amplification components.

B. DUAL-POL END-LAUNCHER MEASUREMENTS

The experimental verification was carried out with two different techniques. The performance of the dual-pol end-launcher was initially assessed using the back-to-back measurement setup illustrated in Fig. 22(a). Two PCB boards were mounted on the same 10-mm-long three-ridge waveguide section. Each of the seven feed elements was connected to a four-port network analyzer. Although this configuration enables straightforward experimental characterization, it inherently suffers from limited accuracy due to systematic errors introduced by the configuration itself [23]. It is not representative of the relevant operative condition because two end-launchers are measured simultaneously (see Fig. 22(a)). For the sake of brevity, only the transmission results are reported hereafter for this setup. The measurement approach in [13] was instead used to accurately characterize the complete $4\times$ 4 scattering matrix of a single end-launcher (two coaxial ports and the two principal polarizations at the common three-ridge waveguide port) as illustrated in Fig. 22(b). The implementation of this measurement setup required the design and fabrication of the dedicated waveguide calibration kit (shown in Fig. 23), composed of matched load, reactive load, $\lambda_{WG}/4$ waveguide section and short circuit. Each calibration standard contains seven elements to allow full characterization of the array prototype. It should be recalled that the method in [13] provides the full scattering matrix of the device-under-test from a set of measurements at the coaxial port only. The standards in Fig. 23 are sequentially connected at the common three-ridge waveguide port without moving or disconnecting the coaxial

This article has been accepted for inclusion in a future issue of this journal. Content is final as presented, with the exception of pagination.

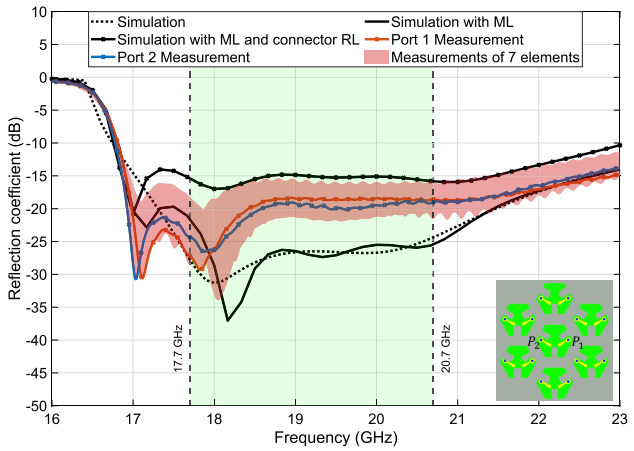

FIGURE 24. Simulated and measured reflection coefficients (S_{11}) and (S_{22}) of the dual-pol end-launcher.

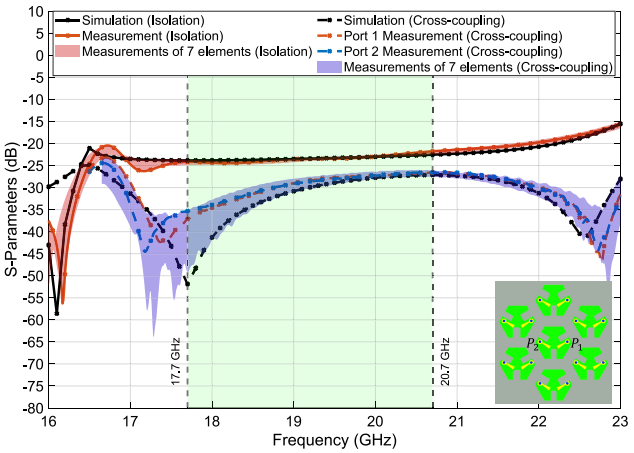

FIGURE 25. Simulated and measured isolation (S_{21}) and cross-coupling coefficient ($S_{3(V)1}$) of the dual-pol end-launcher.

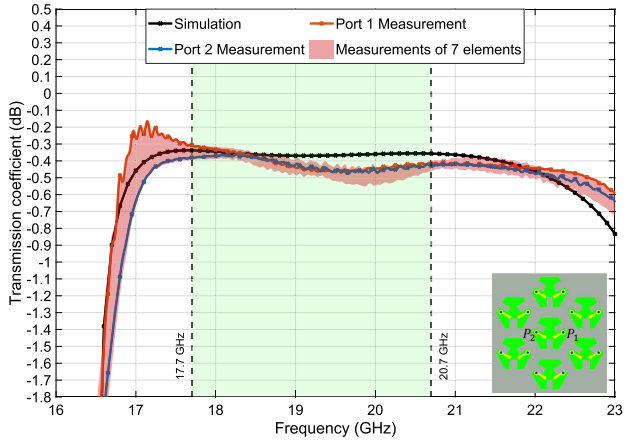

FIGURE 26. Simulated and measured transmission coefficients ($S_{3(U)1}$) and ($S_{3(V)2}$) of the dual-pol end-launcher using the back-to-back measurement configuration.

cables (see Fig. 22(b)). In both measurements approaches the Vector Network Analyzer was previously calibrated by applying the Short-Open-Load-Through technique with the SMPM kit [24].

The comparison between the measured and simulated reflection coefficients is presented in Fig. 24. The dotted black curve corresponds to the simulation of the end-launcher, showing a reflection coefficient below −25 dB over the operational band. The solid black curve shows the simulation of the end-launcher terminated with the waveguide matched load (ML). The red and blue curves with dot markers represent the measured reflection coefficients of the two coaxial ports of the central element, achieving values lower than −18 dB. The shaded red region indicates the variation of the measured reflection coefficient across the complete array, which ranges from −16 dB to −22 dB. This variation is mainly related to the repeatability of the connector placement and soldering.

The observed deviation between simulation and measurements is attributed to the performance of the coaxial connector which was not included in the simulations. For this reason, we determined a simple connector model based on a shunt susceptance of −0.0055 S, corresponding to a reflection coefficient of about −17 dB at 18 GHz [25]. The resulting reflection coefficient (black solid curve with dot markers) agrees well with the worst-case measured result, validating the overall design and modeling approach.

The isolation and cross-coupling performance at the coaxial ports of the dual-pol end-launcher are shown in Fig. 25. Measured and simulated values of the isolation coefficient for the central element are shown in red solid curve with dot markers and black with dot markers, respectively. The slight variation of the measured isolation across the entire array is represented by the red shaded region. The measured isolation is below −23 dB with excellent agreement with the simulation. Measured and simulated values of the cross-coupling for the central-element are shown with red/blue dashed curve and dashed black with dot markers, respectively. The measured results across the array indicated by the blue shaded region show negligible variation among elements. The measured cross-coupling is below −27 dB with excellent agreement with the simulation.

The transmission coefficient of the dual-pol end-launcher is presented in Fig. 26. The simulated response indicates 0.37 dB of total insertion loss across the operational band (black curve with dot markers), including 0.22 dB for the connector loss at 19 GHz [25]. The measurement of the central element provides a maximum value of 0.47 dB at 19.5 GHz (red and blue solid curves with dot markers). The red shadow regions indicate the variation of the measured transmission coefficient across the entire array with small variations up to 0.55 dB at 19.9 GHz. The small ripple is due to both the back-to-back configuration and the residual calibration error. It should be noted that the higher transmission level around 17 GHz for port 1 is correlated with the lower reflection visible in Fig. 24.

The differential phase shift between the transmitted principal polarizations M_X and M_Y is illustrated in Fig. 27. The measured curves of the central element (red and blue solid curves with dot markers) shows good agreement with the simulated results (black solid curve with dot markers). A

This article has been accepted for inclusion in a future issue of this journal. Content is final as presented, with the exception of pagination.

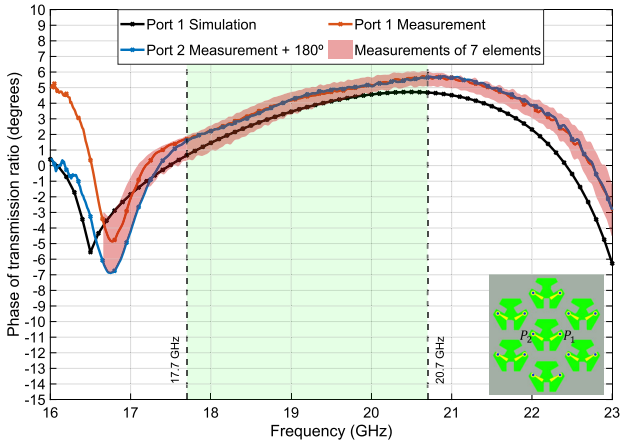

FIGURE 27. Simulated and measured differential phase shift between the transmitted principal polarization M_X and M_Y modes $\phi(S_{3(M_Y)1}) - \phi(S_{3(M_X)1})$ of the dual-pol end-launcher.

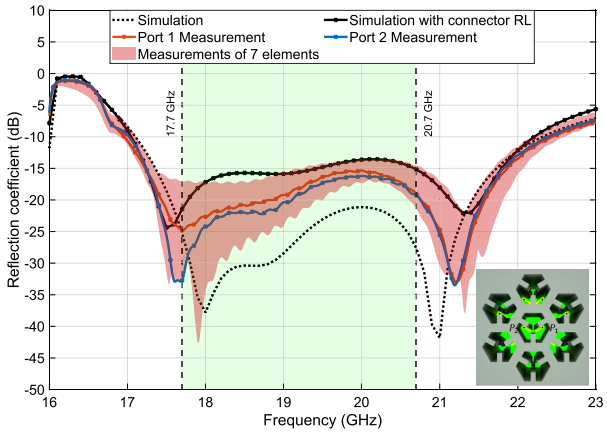

FIGURE 28. Simulated and measured reflection coefficients (S_{11}) and (S_{22}) of the feed element.

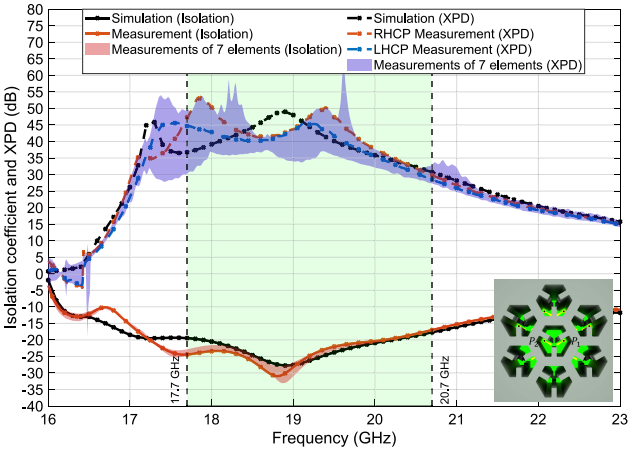

FIGURE 29. Simulated and measured isolation coefficient (S_{21}) and XPD of the feed element.

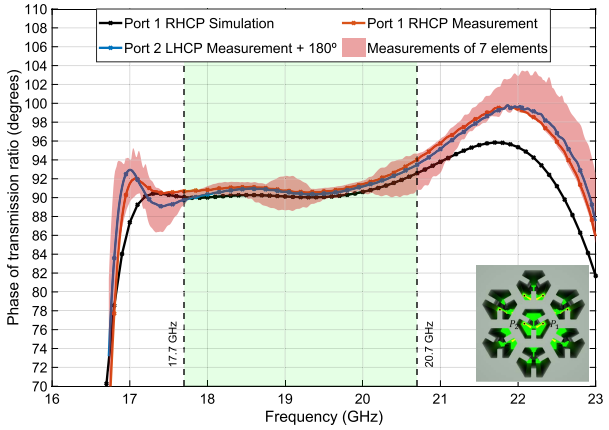

FIGURE 30. Simulated and measured differential phase shift between the transmitted principal polarization M_X and M_Y modes ($\phi_{(Feed\ element)}$) of the feed element.

variation of approximately 1° is observed among the elements (red shaded region).

C. COMPLETE FEED ELEMENT MEASUREMENTS

After characterizing the standalone dual-pol end-launcher, the complete feed element was experimentally evaluated using the technique in [13] and the dual-pol waveguide calibration kit shown in Fig. 23. Simulated and measured reflection coefficients are presented in Fig. 28. The simulated reflection coefficient without connector (dotted black curve) shows −21 dB across the operating band. The simulated effect of the connector produces an increment up to −14 dB (black curve with dot markers). The measured reflection coefficients at coaxial ports 1 and 2 of the central array element (red and blue curves with dot markers) remains below −15 dB showing good agreement with the simulation. The red shaded region indicates the variation of the reflection coefficient across the array elements which is mainly due to connector repeatability.

The isolation coefficient at the coaxial ports and the XPD are presented in Fig. 29. The simulated and measured isolation values are below −18 dB over the operating band (black and red curve with dot markers, respectively). The red shaded region shows a slight variation of the isolation coefficient across the array elements.

The simulated XPD including the connector effect (dashed black curve with dot markers) is higher than 31 dB across the operating band. The measured levels for the central element (blue and red dashed curves with dot markers) are higher than 33 dB up to 20.2 GHz and 29 dB at 20.7 GHz. The blue shaded region indicates the variation across the entire array, which always is higher than 30 dB and 27 dB up to 20.2 GHz and 20.7 GHz, respectively.

The differential phase shift between the principal polarizations M_X and M_Y at the common port is presented in Fig. 30. The simulated results (same as Fig. 15) almost provide a constant 90° up to 20.2 GHz with an increment of 2.5° up to 20.7 GHz (black curve with dot markers). The measured differential phase shift at coaxial port 1 and 2 (red and blue curves with dot markers) are in agreement with the simulation, with a deviation around 1°, which is consistent with the end-launcher data in Fig. 27. The red shaded region indicates

This article has been accepted for inclusion in a future issue of this journal. Content is final as presented, with the exception of pagination.

the slight variation of the differential phase shift across the array elements.

The simulated and measured insertion loss of the complete feed element (not shown for brevity) presents a total loss of 0.6 dB. Considering the connector loss of 0.22 dB, the insertion loss of the proposed feed element is 0.38 dB. The measured isolation between adjacent feed elements at the coaxial ports remains below −70 dB.

V. CONCLUSION

A novel compact feed element for Ka-band downlink DRAs in dual-circular polarization has been presented and validated in this work. The dual circular polarization is achieved by cascading two novel configurations of PCB-to-three-ridge waveguide end-launcher and three-ridge polarizer in hexagonal waveguide.

The end-launcher accommodates two SMPM input ports within the limited inter-element spacing of the DRA (8.96 mm), eliminating the need for additional waveguide expanders or other interconnection layers. The detailed description of the operating principle and reported design guidelines facilitate future adaptation to other geometries. The end-launcher reflection coefficient is slightly constrained by the performance of the selected SMPM connector. Future work will focus on integrating surface-mount SMPM connectors to improve reflection, simplify assembly, and enable automated soldering.

The three-ridge hexagonal waveguide polarizer provides the required 90° differential phase shift between its principal polarizations exploiting both positive and negative stepped variation of the ridge profile. In this way, a compact longitudinal size of 18.75 mm has been achieved. The whole feed element achieves good performance in terms of reflection (−15 dB and −21 dB with and without connector, respectively), isolation (−18 dB), XPD (30 dB) and insertion loss (0.38 dB, without including connector). The proposed solution provides a practical and efficient alternative to conventional OMTs and septum polarizers, offering both reduced size and lower complexity. It does not require full separation of the common waveguide in two halves to provide easier manufacturing and better scaling properties.

The measured reflection coefficient, isolation and XPD of the presented feed element are better than those commonly provided by waveguide-based apertures for DRAs (e.g. −10 dB at ±50° − ±60° scan angles). For this reason, it will not degrade the behaviour of such radiating structures.

In this work, launcher and polarizer were co-designed to achieve a high polarization purity. Future studies will also investigate a joint optimization approach to further enhance performance, particularly in terms of reflection and isolation coefficients. Additionally, redesigning the feed element using additive manufacturing is expected to reduce cost and weight, enabling a monolithic structure. The SMPM connectors could be substituted for soldering pads or short microstrip lines to achieve an even more compact integration to the beamforming integrated circuits.

Additional compactness can be achieved avoiding the waveguide polarizer and inserting a 90° hybrid at the launcher inputs. The combination of such hybrid and the developed dual-pol end-launcher will provide the simultaneous excitation of two orthogonal modes at common port with the required 90° phase shift for circular polarization at the expense of increased losses.

Finally, it should be pointed out that the calibrated feed element presented in this work can be also used to experimentally validate the performance of dual-polarized waveguide radiating elements by connecting them to the three-ridge waveguide common port.

ACKNOWLEDGMENT

Views and opinions expressed are however those of the author(s) only and do not necessarily reflect those of the European Union. Neither the European Union nor the granting authority can be held responsible for them.

REFERENCES

[1] S. D'Addio et al., "Technology developments and R&D activities at the European space agency for satellite communication payloads based on active antennas and digital processors," in *Proc. IEEE Int. Symp. Phased Array Syst. Technol.*, Waltham, MA, USA, 2022, pp. 1–6, doi: 10.1109/PAST49659.2022.9975094.

[2] J. Montgomery, "Ridged waveguide phased array elements," *IEEE Trans. Antennas Propag.*, vol. TAP-24, no. 1, pp. 46–53, Jan. 1976, doi: 10.1109/TAP.1976.1141297.

[3] L. Polo-López, E. Menargues, S. Capdevila, G. Toso, and M. Garcıá-Vigueras, "Solving sub-wavelength lattice reduction in full-metal front-ends for dual-polarized active antennas," *IEEE Trans. Antennas Propag.*, vol. 70, no. 9, pp. 7413–7426, Sep. 2022, doi: 10.1109/TAP.2022.3198512.

[4] D. Pla et al., "High efficiency and circular polarization in SATCOM phased arrays using tri-ridge apertures," *Sci. Rep.*, vol. 14, Aug. 2024, Art. no. 20285, doi: 10.1038/s41598-024-71085-z.

[5] L. Polo-López, L. Berreti, E. Menargues, S. Capdevila, G. Toso, and M. Garcıá-Vigueras, "Dual-polarized spaceborne phased arrays using tri-ridge evanescent waveguide antennas," *IEEE Antennas Wireless Propag. Lett.*, vol. 24, no. 3, pp. 656–660, Mar. 2025, doi: 10.1109/LAWP.2024.3511433.

[6] S. Harms et al., "Waveguide antenna array element with minimized power amplifier load pull for LEO NTNs," in *Proc. 54th Eur. Microw. Conf.*, Paris, France, 2024, pp. 272–275, doi: 10.23919/EuMC61614.2024.10732698.

[7] C. Vazquez-Sogorb, R. Montoya-Roca, G. Addamo, O. A. Peverini, and G. Virone, "Ridged apertures for LEO direct radiating arrays in Ka-band," *MDPI Appl. Sci.*, vol. 14, no. 17, Sep. 2024, Art. no. 7825, doi: 10.3390/app14177825.

[8] E. Menargues, S. Capdevila, M. Vizcarro, M. Billod, I. Bengocchea, and M. Garcıá-Vigueras, "Metal 3D-printed high-performance radiating panel for SATCOM AESA terminals," in *Proc. IEEE Int. Symp. Phased Array Syst. Technol.*, Boston, MA, USA, 2024, pp. 1–5, doi: 10.1109/ARRAY58370.2024.10880436.

[9] N. J. G. Fonseca, "Two-probe waveguide orthomode transducer with twofold rotational symmetry," *IEEE Trans. Microw. Theory Techn.*, vol. 69, no. 7, pp. 3228–3235, Jul. 2021, doi: 10.1109/TMTT.2021.3075957.

[10] L. Wen, Z. Yu, C. Chen, L. Zhu, J. Zhou, and W. Hong, "Design of evanescent quad-ridge antenna with compact transition for 5 G millimeter-wave phased-array applications," *IEEE Antennas Wireless Propag. Lett.*, vol. 22, no. 10, pp. 2532–2536, Oct. 2023, doi: 10.1109/LAWP.2023.3294585.

[11] J. Bornemann, S. Amari, J. Uher, and R. Vahldieck, "Analysis and design of circular ridged waveguide components," *IEEE Trans. Microw. Theory Techn.*, vol. 47, no. 3, pp. 330–335, Mar. 1999, doi: 10.1109/22.750235.

This article has been accepted for inclusion in a future issue of this journal. Content is final as presented, with the exception of pagination.

[12] H. Song, L. Jia, J. Tan, Y. Zhang, and S. Liu, "Design of wideband quad-ridge waveguide polarizer," in *Proc. 4th China Int. SAR Symp.*, Xian, China, 2023, pp. 1–6, doi: 10.1109/CISS60136.2023.10379971.
[13] O. A. Peverini, G. Addamo, R. Tascone, G. Virone, and R. Orta, "Extended through-short-delay technique for the calibration of vector network analyzers with nonmating waveguide ports," *IEEE Trans. Microw. Theory Techn.*, vol. 58, no. 2, pp. 440-450, Feb. 2010, doi: 10.1109/TMTT.2009.2038455.
[14] J. C. Lafond et al., "Thales Alenia space multiple beam antennas for telecommunication satellites," in *Proc. 8th Eur. Conf. Antennas Propag.*, The Hague, Netherlands, 2014, pp. 186–190, doi: 10.1109/EuCAP.2014.6901723.
[15] A. Bhattacharyya, "Array of waveguide horns," in *Phased Array Antennas: Floquet Analysis, Synthesis, BFNs, and Active Array Systems*. Hoboken, NJ, USA: Wiley, 2005, pp. 257–293.
[16] Rogers Corporation, "RO4350B laminates." Accessed: Mar. 2026. [Online]. Available: https://rogerscorp.com/advanced-electronicssolutions/ro4000-series-laminates/ro4350b-laminates
[17] F. Giannini, R. Sorrentino, and J. Vrba, "Planar circuit analysis of microstrip radial stub (short paper)," *IEEE Trans. Microw. Theory Techn.*, vol. TMTT-32, no. 12, pp. 1652–1655, Dec. 1984, doi: 10.1109/TMTT.1984.1132907.
[18] O. A. Peverini, G. Virone, G. Addamo, and R. Tascone, "Development of passive microwave antenna-feed systems for wide-band dual-polarisation receivers," *IET Microw., Antennas Propag.*, vol. 5, no. 8, pp. 1008–1015, Jun. 2011, doi: 10.1049/iet-map.2010.0340.
[19] G. Virone, O. A. Peverini, M. Lumia, G. Addamo, and R. Tascone, "Platelet orthomode transducer for Q-band correlation polarimeter clusters," *IEEE Trans. Microw. Theory Techn.*, vol. 62, no. 7, pp. 1487–1494, Jul. 2014, doi: 10.1109/TMTT.2014.2325793.
[20] G. Virone, O. A. Peverini, M. Lumia, M. Z. Farooqui, G. Addamo, and R. Tascone, "W-band orthomode transducer for dense focal-plane clusters," *IEEE Microw. Wireless Compon. Lett.*, vol. 25, no. 2, pp. 85–87, Feb. 2015, doi: 10.1109/LMWC.2014.2373638.
[21] E. Menargues, M. Garcıá-Vigueras, S. Capdevila, P. Angeletti, and G. Toso, "Meandered waveguides for active antennas," in *Proc. 15th Eur. Conf. Antennas Propag.*, Dusseldorf, Germany, 2021, pp. 1–5, doi: 10.23919/EuCAP51087.2021.9411125.
[22] L. Berretti et al., "Ridged meandered waveguides for 3-D routing and phase delay control and its application to discrete lenses," *IEEE Trans. Antennas Propag.*, vol. 71, no. 5, pp. 4017–4027, May 2023, doi: 10.1109/TAP.2023.3255515.
[23] J. L. Cano and A. Mediavilla, "On the accurate full characterization of septum polarizers through simple amplitude measurements in back-to-back configuration," *IEEE Trans. Microw. Theory Techn.*, vol. 69, no. 1, pp. 179–188, Jan. 2021, doi: 10.1109/TMTT.2020.3020639.
[24] Rosenberger, "18CK010-150 calibration kit." Accessed: Mar. 2026. [Online]. Available: https://products.rosenberger.com/radio-frequency/metrology-measurement-equipment/313480/18ck010-150-calibration-kit?c=22
[25] Rosenberger, "Mini-SMP bulkhead plug hermetic sealed / full detent connector 18S101-5H0E4." Accessed: Mar. 2026. [Online]. Available: https://products.rosenberger.com/radio-frequency/connectors/142498/18s101-5h0e4-bulkhead-plug#



ROGER MONTOYA-ROCA (Member, IEEE) was born in Vic, Spain, in 1998. He received the B.S. and M.S. degrees in telecommunication engineering from the Universitat Autònoma de Barcelona, Bellaterra, Spain, in 2020 and 2022, respectively. In 2023, he started an industrial Ph.D. in electrical, electronics, and communications engineering with the Politecnico di Torino, funded by the European Union's Horizon Europe Marie Sklodowska-Curie Doctoral network ANTERRA (Grant No. 101072363, HORIZON-MSCA-2021-DN-01). He carried out his doctoral work in collaboration with the Applied Electromagnetics Group, National Research Council of Italy (CNR-IEIIT), Turin, and Thales Alenia Space, Rome. His research interests include design of high-performance direct radiating arrays for satellite communication, with particular emphasis on providing compact and novel waveguide components and high-efficiency waveguide radiating elements using additive manufacturing techniques.



CARLOS VAZQUEZ-SOGORB (Graduate Student Member, IEEE) was born in Vila Joiosa, Spain, in 1998. He received the B.S. and M.S. degrees in telecommunications engineering from the Universidad de Alicante, Sant Vicent del Raspeig, Spain, in 2020 and 2022, respectively. He carried out his Master's thesis with Applied Microwave and Computational Electromagnetics Group, University Institute of Physics Applied to Sciences and Technologies, Universidad de Alicante, focusing on the development of millimeter-wave antennas. In 2023, he started an industrial Ph.D. in electrical, electronics, and communications engineering with the Politecnico di Torino, as a Marie Skłodowska-Curie Fellow within the European Union's Horizon Europe Doctoral Network ANTERRA (Grant No. 101072363). His doctoral work is carried out in collaboration with the Applied Electromagnetics Group of the National Research Council of Italy (CNR-IEIIT), Turin, and Thales Alenia Space, Rome. His research interests include design of novel components for satellite antennas, with a focus on high-performance direct radiating arrays employing waveguide and planar technologies, and advanced manufacturing techniques for 6G satellite networks.



FABIO PAONESSA (Member, IEEE) was born in Turin, Italy, in 1985. He received the B.S. and M.S. degrees in biomedical engineering and the Ph.D. degree in electronics engineering from Politecnico di Torino, Turin, Italy, in 2008, 2010, and 2017, respectively. From 2011 to 2012, he was a Research Assistant with Politecnico di Torino, working on electronic systems for therapeutic ultrasound applications. In 2013, he joined the Institute of Electronics, Information and Telecommunications Engineering, Italian National Research Council, Turin, Italy, where he is currently a Researcher. He has authored or coauthored more than 25 journal articles and 50 conference papers. His research interests include UAV-based characterization of antenna systems, including low-frequency radio astronomy arrays, Q-band polarimeters, X-band radar systems, and wireless sensor network nodes. His interests also include the design of microwave waveguide passive components and joint communication and sensing at sub-terahertz frequencies. He has contributed to several national and international research projects. He was the recipient of the Ulrich L. Rohde Innovative Conference Paper Award on Antenna Measurements and Applications, IEEE Antennas and Propagation Society, at the 2018 IEEE Conference on Antenna Measurements and Applications, and Best Student Paper Award at the 36th European Space Agency Antenna Workshop on Antennas and RF Systems for Space Science.



MAURO LUMIA (Member, IEEE) was born in Turin, Italy in 1983. He received the M.S. degree in mechanical engineering and the Ph.D. degree in electronic engineering from the Politecnico di Torino, Turin, Italy, in 2012 and 2017, respectively. In 2013, he joined the Applied Electromagnetics and Electronic Devices Group, CNR-IEIIT, as a Research Fellow, where he is currently a Researcher. His research focuses on advanced manufacturing processes and materials for the next generation of waveguide components.

This article has been accepted for inclusion in a future issue of this journal. Content is final as presented, with the exception of pagination.



GIUSEPPE ADDAMO (Member, IEEE) was born in Messina, Italy, in 1979. He received the Laurea degree (summa cum laude) in electronic engineering and the Ph.D. degree in electronic and communication engineering from the Politecnico di Torino, Turin, Italy, in 2003 and 2007, respectively. In 2007, he joined the Istituto di Elettronica e di Ingegneria dell'Informazione e delle Telecomunicazioni, Consiglio Nazionale delle Ricerche, Turin, as a Research Fellow, where he is currently a Senior Researcher. He holds practical classes in courses on electromagnetic field theory and mathematical analysis with Politecnico di Torino. His research interests include microwave leaky antennas, dielectric radomes, high-power feed systems (such as orthomode transducers (OMTs) and microwave filters), corrugated and smooth wall horns, frequency-selective surfaces, and large dielectric radomes.



OSCAR A. PEVERINI (Member, IEEE) was born in Lisbon, Portugal, in 1972. He received the Laurea degree (summa cum laude) in telecommunication engineering and the Ph.D. degree in electronic engineering from Politecnico di Torino, Turin, Italy, in 1997 and 2001, respectively. During his Postdoctoral studies, he was a Visiting Researcher with the University of Paderborn, Paderborn, Germany, where he was involved in the design of acousto-optical devices. In 2001, he was a Research Fellow with the Physics Department, Politecnico di Torino, and IRITI Institute of the National Research Council of Italy. In 2001, he joined CNR-IEIIT Institute, where he is currently the Director of Research and Coordinator of the Applied Electromagnetics and Electronic Devices Research Unit. Since 2015, he has been a Research Associate with Italian Space Agency. He has been the Technical Manager of several projects aimed at the development of microwave and millimeter-wave devices for space-born applications. He has authored or coauthored more than 50 journal articles, 110 conference papers, and he is a co-inventor of 3 European patents. He has been a Reviewer of several journals and conferences in the microwave area. From 2018 to 2021, he was the President of the Evaluation Board for the Research and Development Projects submitted in the ICT area within the calls of the Fund for Sustainable Growth Programme of the Italian Ministry of Economic Development.



DAVIDE MAIARELLI (Member, IEEE) was born in Perugia, Italy, in 1971. He received the Laurea degree (cum laude) in electronic engineering from the University of Perugia, Perugia, Italy, in 2001. From 2001 to 2015, he was with Thales Alenia Space-Italy (formerly Alenia Spazio S.p.A.), Rome, as Senior Antenna and RF engineer, Antenna System Engineer and Project Manager. He worked on a number of commercial, institutional and research projects designing and developing satellite antenna systems and microwave passive components. He participated in several research activities concerning modelling techniques for microwave/antennas components and numerical EM methods, in collaboration with Italian universities. From 2015 to 2021, he was with Airbus DS Italy, Rome, as Technical Manager and Head of the Antennas and RF Passive Engineering group, working as RF design, technical and program Manager of several satellite components, feed chains and filters. In 2021, he re-joined Thales Alenia Space-Italy, where he is currently Head of Antenna RF Engineering team, deeply involved in antenna design and development for space applications.



GIUSEPPE VIRONE (Senior Member, IEEE) was born in Turin, Italy, in 1977. He received the Laurea degree (summa cum laude) in electronic engineering and the Ph.D. degree in electronics and communication engineering from the Politecnico di Torino, Turin, Italy, in 2001 and 2006, respectively. He is currently the Director of Researcher with the Istituto di Elettronica e di Ingegneria Informatica e delle Telecomunicazioni (IEIIT), Italian National Research Council, Turin. He joined IEIIT, as a Research Assistant in 2002. He coordinated more than 25 scientific projects/research units/work-packages funded by both the industry and other scientific research organizations and joined more than 30 research projects as a collaborator. He authored 60 journal papers, 120 conference papers, and three European patents. His activities concern the design, numerical analysis, and characterization of microwave, millimeter passive components and sub-THz components for feed systems, antenna arrays, frequency selective surfaces, compensated dielectric radomes for communication and sensing applications. He is also active in advanced signal processing and propagation measurements for smart radio environments and non-terrestrial networks.